Materials & Design 258 (2025) 114694

Contents lists available at ScienceDirect

Materials & Design

journal homepage: www.elsevier.com/locate/matdes

A hierarchically structured fibrous sensor with temperature-responsive adhesion for wearable applications

Xiaodong Wang [a,b], Ziqian Bai [a,b,*], Kai Lin [a,b], Hongci Hu [a,b,c]

[a] School of Automation and Intelligent Manufacturing, Southern University of Science and Technology, Shenzhen 518055, China
[b] Guangdong Provincial Key Laboratory of Fully Actuated System Control Theory and Technology, Southern University of Science and Technology, Shenzhen 518055, China
[c] School of Fashion and Textiles, The Hong Kong Polytechnic University, Hung Hom, Kowloon, 999077, Hong Kong, China

ARTICLE INFO

Keywords:
Wearable sensor
Self-adhesion
Breathable
Controllable adhesion
Electrospinning

ABSTRACT

Flexible self-adhesive wearable strain sensors have attracted significant attention for their ability to conform closely to human skin and accurately capture physiological signals. However, many existing designs struggle to balance sensing performance with essential comfort-related features such as breathability, waterproofness, and on-demand removability. This paper reports a hierarchically structured nanofiber-network strain sensor fabricated via electrospinning, integrating three layers: a sensing layer, a spacer layer, and an adhesive layer. The all-fiber architecture provides excellent flexibility, stretchability, and environmental adaptability, which can closely mimick the mechanical properties of human skin. The sensing layer is composed of multi-walled carbon nanotubes/carbon black/thermoplastic polyurethane (MWCNT/CB/TPU), which can exhibit high sensitivity, linearity, rapid response time (130 ms), and excellent cycling stability (2,000 cycles). The adhesive layer, made of electrospun poly(N,N-dimethylacrylamide, PDMA) nanofibers, forms a strong interface with the skin through hydrogen bonding and van der Waals interactions, maintaining adhesion even in humid conditions. Incorporating phase-change monomers such as octadecyl acrylate and lauryl acrylate yields a melting point of ~38.1 °C, enabling reversible, temperature-triggered detachment. This work addresses the challenge of combining high performance with comfort, representing a paradigm shift in wearable sensing by enabling imperceptible monitoring and broadening applications in personal healthcare and interactive electronics.

1. Introduction

With the rapid advancement of flexible electronics, flexible strain sensors have shown great potential in wearable applications such as health monitoring [1–3], motion detection [4–6], and human machine interaction [7–9] owing to their outstanding mechanical flexibility and high sensitivity [10–12]. Previous studies have demonstrated that achieving conformal contact between the sensor and the skin is essential for ensuring accurate motion detection [13–15]. However, conventional flexible sensors typically rely on external fixation methods (e.g., adhesive tapes or bandages) to attach to the body, which leads to several limitations [16–18]. First, human skin exhibits unique microscopic topographical features and dynamic deformations [19–21], with a maximum strain of up to 55 % [22,23], making it difficult for traditional fixation approaches to maintain stable and intimate contact. Second, joint movements generate complex mechanical forces that may lead to sensor displacement or detachment [24,25]. More importantly, perspiration during physical activity significantly substantially reduces interfacial adhesion, thereby compromising the reliability of signal acquisition [26,27]. To address these challenges, the next generation of flexible sensors are expected to integrate self-adhesion, breathability, water resistance, and tunable adhesion properties. These features not only ensure stable conformal contact but also enable long-term and continuous wearability, thus providing a solid foundation for the practical implementation of wearable devices.

Most existing strain sensors are fabricated by integrating polymeric elastomers with conductive materials, and their self-adhesion, breathability, and water resistance largely depend on the properties of the selected elastomer [28–31]. Hydrogels, owing to their excellent mechanical flexibility and intrinsic adhesive properties, have been considered ideal candidates for self-adhesive sensor substrates [17,32–35]. Although strategies such as dynamic covalent bond

* Corresponding author at: School of Automation and Intelligent Manufacturing, Southern University of Science and Technology, Shenzhen 518055, China.
E-mail address: baizq@sustech.edu.cn (Z. Bai).

https://doi.org/10.1016/j.matdes.2025.114694
Received 15 July 2025; Received in revised form 25 August 2025; Accepted 3 September 2025
Available online 4 September 2025

engineering, modulation of intermolecular interactions, and polymer chain modification have enabled tunable adhesion and enhanced stability under complex conditions, hydrogels still suffer from a fundamental limitation [36,37]. Specifically, repeated operation leads to water loss, resulting in performance degradation and severely limiting long-term stability [38–40]. Therefore, the development of new elastomeric systems with improved mechanical robustness, environmental stability, and controllable adhesion remains a key research focus in the field of flexible sensor technology.

Electrospinning is an efficient technique for fabricating micro/nanofiber structures. It enables the production of nonwoven elastomeric membranes with three-dimensional porous networks similar to those found in hydrogels [41–44]. This unique fibrous architecture not only provides continuous channels for moisture and air transport but also replicates the multilayer collagen fiber weave of human skin [45–47], thereby imparting inherent waterproofness, breathability, and mechanical adaptability to strain sensors [48–50]. The integration of hydrogel adhesives with electrospinning technology thus offers a promising strategy to overcome the intrinsic limitations of conventional hydrogels, particularly the degradation in performance caused by water loss during prolonged use [51–54]. This approach paves the way for developing next-generation flexible strain sensors tailored for wearable applications. At present, most hydrogel–electrospun composites are fabricated via spray-coating techniques, where the hydrogel adhesive is applied onto electrospun membranes [55]. However, this approach clogs the nanofiber network, compromising its inherent porosity and air permeability [56]. Moreover, the strong interfacial adhesion of hydrogel adhesives may cause skin irritation or even injury during detachment, undermining both safety and comfort. Therefore, a key challenge in this field is to design new material systems and structural architectures that combine the functional advantages of hydrogels with the porous features of electrospun networks. Such strategies are essential for developing skin-friendly, breathable, and reversibly adhesive elastomers suited for long-term wearable applications.

In this study, we developed a self-adhesive flexible strain sensor with a hierarchical fibrous network structure, consisting of a sensing layer, a spacer layer, and an adhesive layer, fabricated via electrospinning. Benefiting from its all-fiber architecture, the sensor exhibits excellent waterproof performance (contact angle of 107°), breathability (0.06 kPa·S/m), and mechanical adaptability, which significantly enhances long-term adhesion stability (over 3 days) and wearing comfort. To achieve thermally tunable adhesion, phase-change monomers (octadecyl acrylate and lauryl acrylate) were incorporated into the adhesive layer. Through molecular chain engineering, the phase transition temperature was precisely tailored to 38.1 °C, enabling on-demand, nondestructive detachment near skin temperature and minimizing irritation during repeated use. The optimized interface exhibits a robust adhesion strength of up to 118 N/m on human skin, facilitating reliable acquisition of complex biomechanical signals such as joint motion. Coupled with a convolutional neural network (CNN) model, the sensor demonstrates high-accuracy classification (training accuracy of 92.2 %) of multiple joint movement patterns. Furthermore, integration with a printed circuit board (PCB) enables real-time mapping of body motion to virtual control commands, showcasing its potential for interactive human–machine interfaces. This work introduces a multifunctional fibrous sensing platform that bridges high-performance strain sensing with tunable adhesion and wearing comfort. The synergistic design strategy provides a promising route toward next-generation wearable electronics for applications in smart healthcare and immersive virtual environments.

2. Experimental procedure

2.1. Materials

Thermoplastic polyurethane (TPU, C180A) was purchased from BASF, China. N, N-dimethylacrylamide (DMAA), tetrahydrofuran (THF), 2-Hydroxy-4′-(2-hydroxyethoxy)-2-methylpropiophenon, dimethyl formamide (DMF) and ethyl acetate (EA) were purchased from Aladdin, Shanghai, China. Carbon black (CB, K90) was purchased from Rhawn, Shanghai, China. Multi-walled carbon nanotubes (MWCNTs, length 3–12 μm, diameter 3–5 nm) and lauryl methacrylate were purchased from Macklin, Beijing, China. Octadecyl acrylate was purchased from RHAWN, Shanghai, China.

2.2. Preparation of flexible sensor

2.2.1. Fabrication of TPU nonwoven textiles

The TPU nonwoven textiles were fabricated by an electrospinning equipment (Model TEADFS-700, Beijing Xinrui Baina Technology Co., LTD). Firstly, TPU solution with a concentration of 15 wt% was prepared by dissolving a specific amount of TPU particles into DMF/THF mixture solution with a volume ratio of 1:1 under stirring for 12 h at room temperature (as shown in figure S1). Then, the obtained TPU solution was transferred to a disposable syringe (needle: 19G) with a capacity of 10 mL and simultaneously electrospun on a conductive aluminum foil. The electrospinning parameters were set as follows: a voltage of 20 kV, the syringe propulsion rate at 0.02 mL/min, the distance between the syringe needle and the collecting roller at 15 cm, the rolling speed of receiver was 100 rpm, the ambient temperature at 26 °C, the humidity at 45 % RH and spinning duration for 4 h.

2.2.2. Preparation of MWCNT/CB/TPU textile-based sensor

Typically, 0.25 g MWCNT and various amounts of CB were respectively added into 50 mL deionized water. MWCNT/CB hybrid dispersions with CB concentrations of 1, 2, 3, 4, and 5 mg/mL were obtained via probe sonication (360 W, intermittent mode) for 1 h in an ice bath. After that, electrospun TPU nonwoven textiles with an average thickness of 100 μm was cut into pieces with the size of 60 × 60 mm^2, which were then immersed in the above MWCNT/CB dispersion for 30 min in the ultrasonic bath for the assembly of CB/CNT hybrids. Finally, the wet nonwoven textiles were vacuum dried at 60 °C for 6 h, and TPU electrospun on the dried nonwoven textiles for 1 h (The electrospinning parameters are shown in 2.2.1).

2.2.3. Preparation of self-adhesive layer

The PDMA solution was prepared by mixing EA, DMAA, octadecyl acrylate, lauryl methacrylate, 2-hydroxy-4‘-(2-hydroxyethoxy)-2-methylpropiophenon was stirred under 365 nm UV lamp for 12 h with the solid content ratio of 25: 24:38:17:1(as shown in Fig. S1). Then, the obtained PDMA solution was transferred to a disposable syringe (needle: 19G) with a capacity of 10 mL and electrospun on TPU/MWCNT/CB sensing layer TPU surface (prepared in section 2.2.2) for 1 h at the same time. After electrospinning of PDMA layer and drying in the oven at 50°C, the flexible sensor was prepared.

2.3. Characterizations and measurements

2.3.1. Morphological and structural characterization

The morphology of TPU nonwoven textiles and self-adhesive layer was observed by a high resolution scanning electron microscope (SEM, FEI APREO S) with an acceleration voltage of 15 kV. The surface of the sample was sputtered with platinum gold before SEM observation. The element distribution of TPU nonwoven textiles and self-adhesive layer was observed by energy dispersive spectrometer (EDS, 550i). The morphology and surface roughness of self-adhesive layer were measured by atomic force microscopy (AFM). The contact angle between water and sweat and the self-adhesive layer was measured by video optical contact Angle (DSA25). The melting and crystallization temperature of the self-adhesive layer were measured by differential scanning calorimetry (DSC) at a heating rate of 5 °C/min, with a temperature range from 0 °C to 50 °C.

2.3.2. Adhesive force test of self-adhesive sensor

The adhesive force of the self-adhesive sensor was tested by a flexible multimodal testing system. Firstly, Placed the customized PTFE, glass, metal, and silicone plates on a heating stage, and maintain them at a constant temperature of 50 °C. Then, cut the self-adhesive sensor into a small sheet of 100 × 10 mm^2 and press the self-adhesive layer on a heated PTFE plate (contact area of 10 × 10 mm^2) until cooled to room temperature. After that, the clamp of the flexible multimodal test system clamped the sensor and PTFE plate respectively and performed horizontal and vertical adhesion tests at a shear speed of 20 mm/min. Finally, the adhesive force was tested by spraying artificial sweat on a PTFE plate heated to 50 °C. Similar methods were used to test the adhesion of self-adhesive sensors on Glass, Metal and silicone plates.

2.3.3. Air permeability test of self-adhesive sensor

The permeability of the self-adhesive sensor was tested by an automatic air-permeability tester. Air permeability is indicated by the air resistance value (R_a), the smaller the R_a value, the better the air permeability. R_a is obtained by pressure/rate of air flow as electrical resistance calculation while this tester has constant rate of air flow and pressure has linear relation with Ra, Ra is calculated from pressure difference.

$$R_a = \Delta P / V$$

In the above equation, ΔP represents the pressure difference (Pa), V represents rate of air flow per unit area($m^3/m^2 \cdot S$).

2.3.4. Sensing performance test of self-adhesive sensors

The sensing performance of the self-adhesive sensor was tested by a high-precision source meter and a flexible multimodal test system. First, the clamp of the flexible multimodal test system was used to clamp both ends of the sensor and perform stress–strain tests at a tensile rate of 20 mm/min. Secondly, the 5 cycles tensile tests with strain range of 1–100 % were conducted to test the working range of self-adhesive sensor. Meanwhile different strains from 1 % to 100 % were applied and the relative resistance was recorded using a high precision original meter. Finally, the 2000 cycles of tensile tests with 20 % strain were conducted to test the durability of self-adhesive sensor. In terms of human–computer interaction, the sensor was heated to 50 °C using a heating table, and then the self-adhesive layer was pressed on the skin until it cooled to room temperature. Then collected the signals of fingers and knees under different movements and transmitted them to the computer through the PCB board. Finally, the control of the game character was achieved by determining whether the signal exceeds the threshold. Testing the wearables was carried out with the assistance of a human participant volunteer (an author of this article), and informed written consent was obtained from the participant.

3. Results and discussion

3.1. Preparation and characterization of sensors

The self-adhesive flexible sensor is constructed using a tri-layer electrospun membrane architecture, consisting of a sensing layer, a spacer layer, and an adhesive layer (Fig. 1a). The fabrication process is as follows: Firstly, the electrospun TPU film (detailed in Fig. S1) was immersed in MWCNT/CB dispersion solution, and the sensor layer was formed after ultrasonic stirring and drying. Subsequently, short time TPU electrospinning was performed on either side of the sensing layer to prepar the spacer layer. Finally, a copolymer (PDMA) solution of DMAA, octadecyl acrylate, lauryl methacrylate and 2-hydroxy-4 '-(2-hydroxyethoxy) −2-methylphenylacetone (detailed in Fig. S1) was electrospun onto the spacer layer to form the adhesive layer. To evaluate the biocompatibility of the sensor, mouse embryonic fibroblasts (MEFs) were cultured in a solution containing PDMA for 24 h and the cell activity was analyzed. The results demonstrated that PDMA had excellent biocompatibility biocompatibility [39,56]. Meanwhile, octadecyl acrylate and lauryl methacrylate in PDMA give the adhesive layer excellent waterproof performance, consequently the sensor retains performance in wet environment. In addition, octadecyl acrylate in PDMA crystallizes

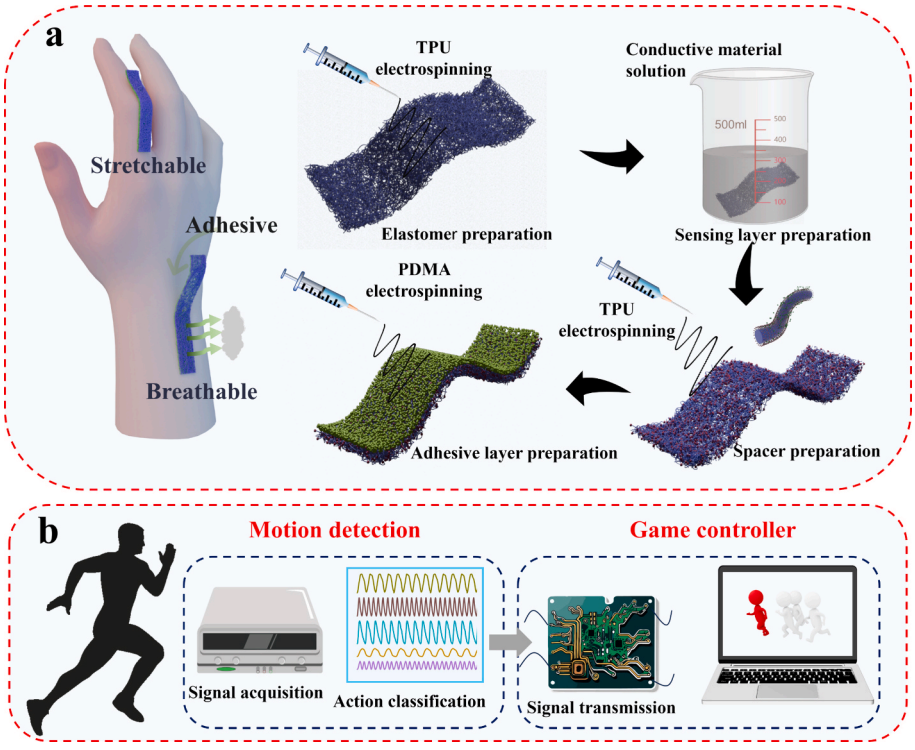

Fig. 1. a) Schematic illustration of the preparation procedures of self-adhesive flexible sensor. b) Schematic illustration of the sensor's applications in human motion detection and game controller.

at room temperature and meltes when the temperature rose to a certain threshold, which enabled the adhesive layer to be stripped without damage through temperature control. The all-fiber structure film constructed by electrospinning technology also provides good air permeability for the sensor, ensuring long-term wearing comfort. Based on the above characteristics, the self-adhesive flexible sensor prepared can stably adhere to the skin surface for a long time and maintain conformal contact with the skin, thus accurately collecting human movement signals (Fig. 1b). The acquired signals not only reflect the motion states of human joints but can also be transmitted to a computer via a PCB, enabling motion-to-game mapping (Fig. 1b).

The self-adhesive sensor developed in this study consists of a sensing layer, a spacer layer, and an adhesive layer, with corresponding photographs and cross-sectional microstructures shown in Fig. S2 and Fig. 2a, respectively. The sensing layer was fabricated via an ultrasonic dip-coating process, in which the conductive MWCNT/CB composite was uniformly integrated with the three-dimensional porous TPU fibrous film (Fig. 2b). From the SEM image of the sensing layer (Fig. 2c), it can be observed that the MWCNT/CB composite is uniformly and densely coated on the surface of the TPU fibers. Meanwhile, the microporous structure of the TPU membrane is largely preserved, with only negligible blockage and aggregation phenomena observed. High-magnification SEM imaging (Fig. 2c) reveals that the MWCNT/CB composite forms a uniform and continuous conductive network on the surface of the TPU fibers. The sensing mechanism of this layer can thus be described as follows: upon external tensile loading, the TPU fibrous matrix undergoes deformation, inducing reversible structural changes in the surface-bound MWCNT/CB network, which in turn corresponding variations in electrical resistance. Notably, during stretching, CB particles serve as dynamic bridging points between adjacent MWCNTs (as shown in Fig. S3). This unique "point-to-line" hybrid conductive architecture not only preserves the integrity of the conductive pathways but also significantly broadens the working strain range of the sensor.

The spacer layer is also fabricated from TPU fibrous film, whose three-dimensional network structure ensures the sensor's breathability. The adhesive layer is fabricated by electrospinning PDMA material onto the surface of the spacer layer, forming a beaded three-dimensional network structure (Fig. 2d). This unique morphology results from the high surface tension and low viscosity characteristics of the PDMA and EA solution. To confirm the presence of PDMA, elemental (C, N, O) energy-dispersive X-ray spectroscopy (EDS) analysis was performed on both the spacer and adhesive layers. As shown in Fig. 2e, Figures I and III present the SEM images of the spacer and adhesive layers, respectively, while Figures II and IV display their N element distribution (The

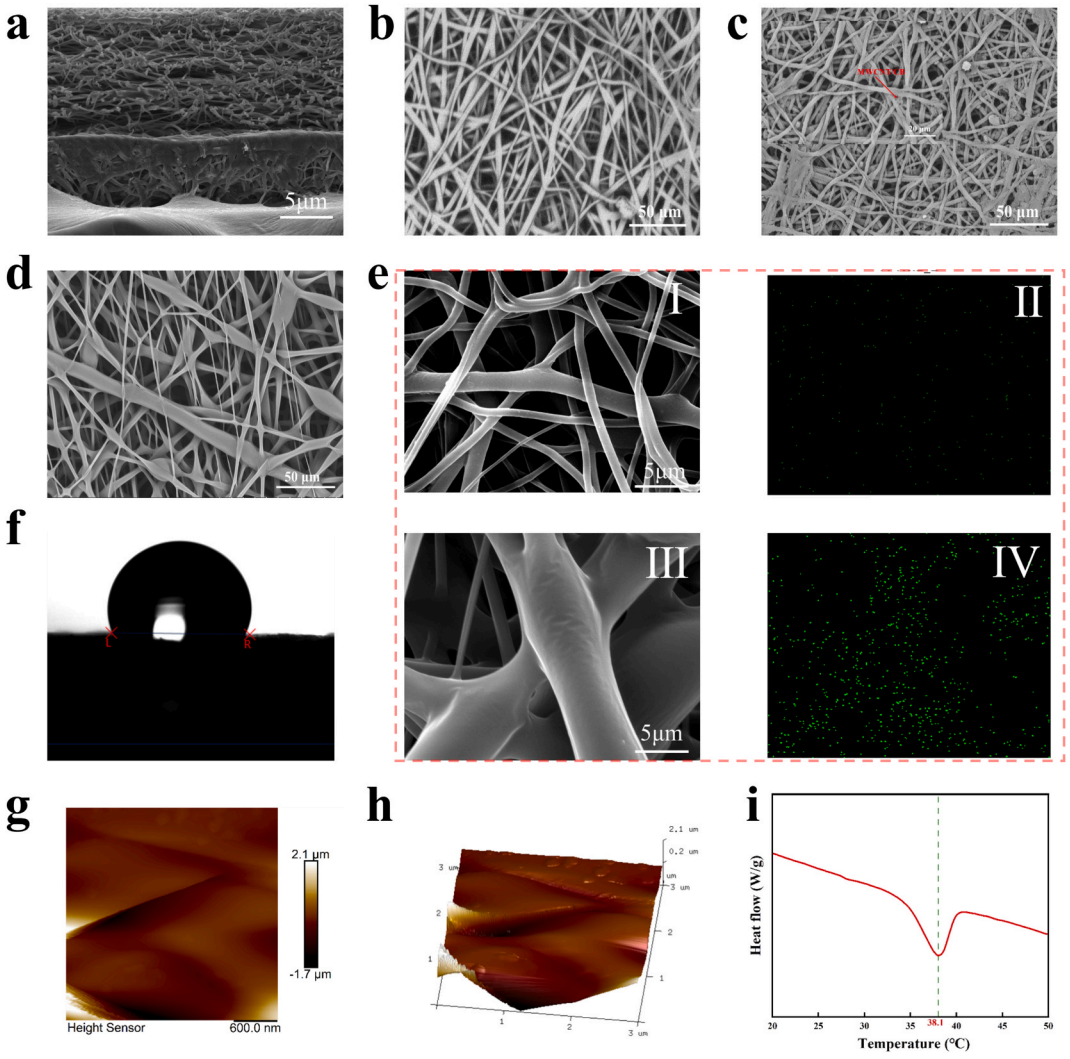

Fig. 2. Material structure and performance characterization of the self-adhesive flexible sensor. SEM image of a) the sensor cross section, b) the distribution of TPU fibers in the sensing layer, c) the microstructure of the TPU/MWCNT/CB composite fibers in the sensing layer, d) the fiber structure in the adhesive layer. e) SEM images of the spacer and adhesive layers (I and III) with corresponding EDS elemental analysis (II and IV). f) Hydrophobicity test of the adhesive layer. g) Surface roughness measurement of the adhesive layer—2D planar view and h) 3D planar view. i) DSC scan of the adhesive layer.

elemental distributions of C and O are presented in Fig. S4). Due to the significantly higher nitrogen content in PDMA compared to TPU, the brightness of Figure IV is notably higher than that of Figure II. Additionally, the presence of stearyl methacrylate and lauryl methacrylate in PDMA imparts hydrophobic properties, with a water contact angle reaching 107.2° (Fig. 2f). The electrospun PDMA network structure also allows for the free diffusion of moisture from both the skin and the environment through the pores, ensuring excellent adhesion in humid conditions while maintaining breathability. To ensure intimate contact between the sensor and the skin, this work tested the surface roughness of the adhesive layer. The results indicatethat the sensor surface is smooth and uniform (Fig. 2g and h), which aids in the uniform distribution of force during stretching, thus enabling more accurate reflection of human motion. Then, to achieve secure adhesion and controlled detachment, the melting temperature of the PDMA adhesive layer was carefully regulated. Studies indicate that the melting temperature of PDMA is primarily controlled by the stearyl methacrylate content, with the formulation optimized to adjust the melting temperature to 38.1 °C or higher (Fig. 2i). When the temperature exceeds the melting point, PDMA partially melts and penetrates the skin surface; after cooling and solidifying, it provides strong adhesion. Therefore, to ensure reliable use, the melting temperature of PDMA should be higher than body

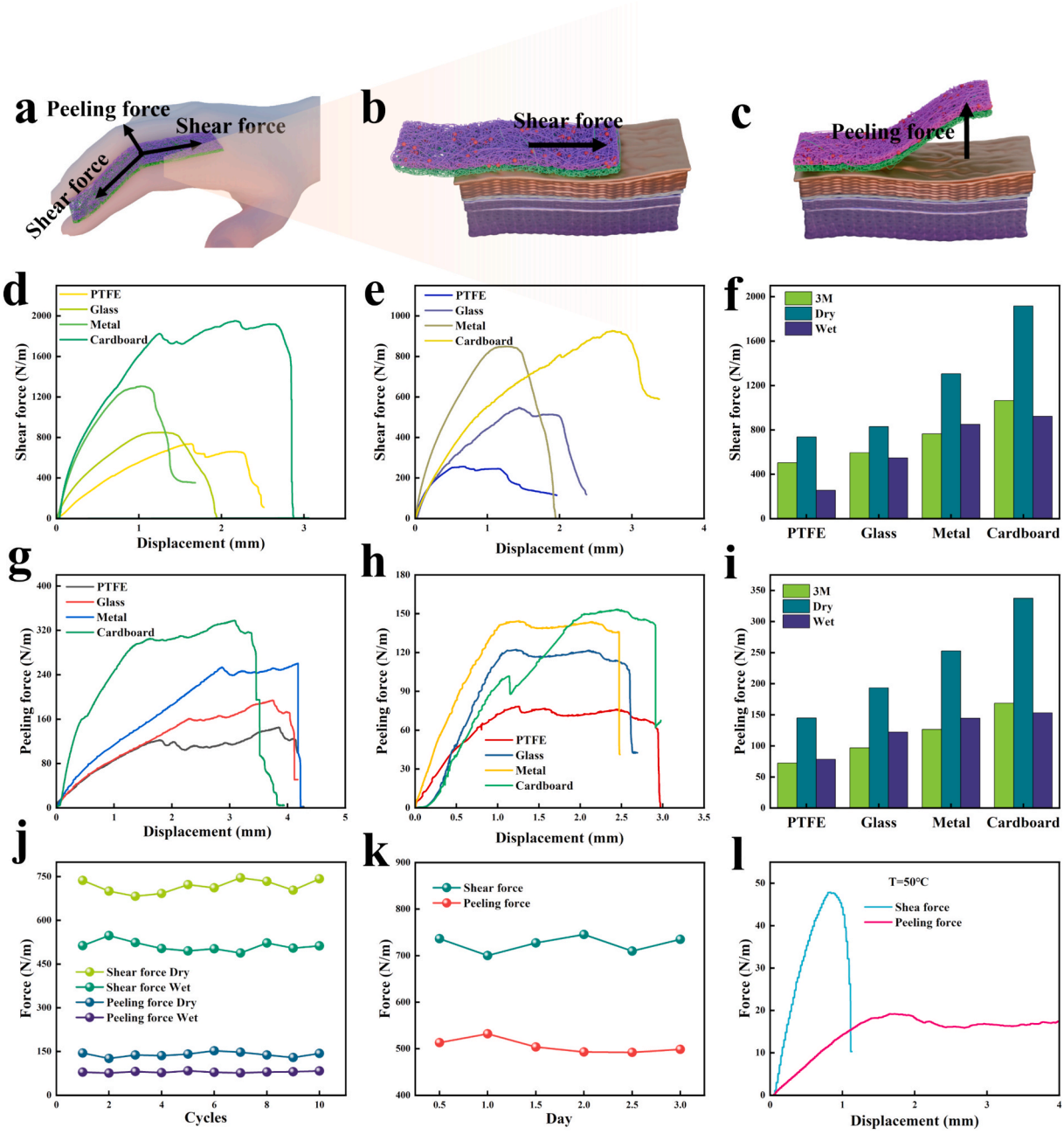

Fig. 3. a) Force analysis diagram of the self-adhesive flexible sensor on a bent finger joint. The sensor subjected to b) horizontal shear force and c) vertical peel adhesion force on the skin. Adhesion performance tests of the sensor on various substrates (PTFE, Glass, Metal, and Cardboard). Horizontal shear force of the sensor on each substrate under d) dry and e) humid conditions, respectively. f) Comparison of the horizontal shear force between 3 M tape and the sensor on each substrate. Peel adhesion force of the sensor on each substrate under g) dry and h) humid conditions, respectively. i) Comparison of the peel adhesion force between 3 M tape and the sensor on each substrate. j) Adhesion strength of the sensor on the PTFE substrate after 10 cyclic test and k) 3-day cycle test on the PTFE substrate. l) Adhesion test of sensor on PTFE substrate at 50 °C.

temperature, while the crystallization temperature should be below body temperature. Finally, the intermediate layer successfully achieves physical separation between the adhesive and sensing layers, effectively preventing the melted PDMA from infiltrating the sensing layer and compromising the sensor's performance.

3.2. Self-adhesive properties

When applied to human joints (e.g., fingers), the sensor inevitably experiences frictional forces and normal pressure from the skin, which may cause relative displacement between the sensor and the skin. For analytical convenience, these forces can be simplified into shear force in the horizontal direction and peel force in the vertical direction, as illustrated in Fig. 3a. Additionally, the sensor may be exposed to humid environments, such as perspiration or external moisture. In daily life, sweat and other secretions increase skin surface humidity, thereby affecting the adhesion performance of the sensor. To comprehensively evaluate its adhesive performance, both shear force (Fig. 3b) and peel force (Fig. 3c) were measured under dry and wet conditions. For adhesion testing, PTFE, glass, metal, and cardboard were selected as substrates, and a self-adhesive sensor with dimensions of 100 × 10 mm^2 was used. The shear force testing procedure was as follows: first, each substrate was heated to 50 °C using a temperature-controlled heating stage. The adhesive layer of the sensor was then attached to the substrate (contact area: 10 × 10 mm^2), followed by continued heating for a specified period before turning off the power. After the substrate and sensor cooled to room temperature, shear force testing was conducted under both dry and humid conditions using a flexible electronic multimodal testing system (Shear force test diagram as shown in Fig. S5a). Results are presented in Fig. 3d and 3e. Under dry conditions, the shear forces of the sensor on PTFE, glass, metal, and cardboard substrates were 736.84, 829.36, 1305.42 and 1916.72 N/m, respectively. Under humid conditions, these values were reduced to 256.16, 547.76, 849.36 and 922.38 N/m, respectively. To further assess performance, the shear force of commercial 3 M adhesive tape on these substrates was also measured (Fig. S5b). As shown in Fig. 3f, the shear force of the self-adhesive sensor was approximately twice that of 3 M tape under dry conditions, whereas under wet conditions, the two exhibited comparable performance.

The peel adhesion testing method was similar to that of shear force testing, with the primary difference being that the direction of the applied force was changed from horizontal to vertical (as shown in Fig. S6a). The test results, presented in Fig. 3g and 3 h, revealed that in the dry environment, the peel adhesion forces for the sensor on each substrate were 144.90, 193.40, 252.84 and 337.48 N/m, respectively. In the wet environment, the peel adhesion forces were 78.22, 122.27, 144.40 and 153.22 N/m. For comparison, the peel adhesion of commercial 3 M adhesive tape was also measured on the same substrates (Fig. S6b). As shown in Fig. 3i, under both dry and wet conditions, the peel adhesion force of the sensor was significantly greater than that of the commercial 3 M tape. To evaluate the adhesion stability of the sensor, a 10-cycle test was conducted on the sensor adhered to a PTFE substrate. As shown in Fig. 3k, the adhesion strength exhibited minimal variation across cycles (data fluctuation of less than 2.9 %), indicating excellent cyclic stability. In addition, the long-term adhesion performance was assessed by measuring the peel strength after the sensor was attached to the PTFE substrate for different durations. Even after 3 days, the adhesion remained stable, with deviations of less than 2.7 % (as shown in Fig. 3J), demonstrating the sensor's reliability for prolonged use. Finally, to evaluate the effect of temperature on the adhesive performance of the sensor, tests were conducted at 50 °C. As shown in Fig. 3l, the sensor exhibited a shear force of 36.71 N/m and a peel force of 19.51 N/m at this temperature—both markedly lower than the values measured at room temperature. This result confirms that temperature modulation enables controllable detachment of the sensor, offering a reliable strategy for on-demand removal in practical applications.

Analysis of the experimental data reveals that the adhesive strength of the sensor varies across different substrates. This variation arises because the adhesive performance of PDMA primarily depends on van der Waals interactions between its side chains (octadecyl acrylate and lauryl methacrylate) and the substrate surfaces[39]. As discussed in Section 3.1, when the temperature exceeds 38.1 °C, PDMA enters a molten state. Therefore, when both the substrate and sensor are heated to 50 °C, the sensor's adhesive layer softens, forming conformal contact with the substrate surface. The rougher the substrate surface, the greater the contact area between the sensor and substrate, resulting in stronger van der Waals forces and a significant increase in shear and peel adhesion forces. However, environmental humidity adversely affects adhesion performance. Moisture adsorption on the substrate surface reduces the effective contact area between the sensor and substrate, thereby weakening interfacial adhesion. In addition, prolonged exposure to elevated temperatures compromises adhesion by intensifying the thermal motion of PDMA molecular chains, which disrupts intermolecular interactions and significantly attenuates van der Waals forces. To achieve optimal adhesion, a temperature-regulated bonding protocol is recommended: heat the substrate above the melting point of PDMA (>38.1 °C) to promote softening and intimate contact, followed by controlled cooling to stabilize intermolecular interactions. This approach facilitates the formation of a robust adhesive interface between PDMA and the substrate, ultimately enhancing the sensor performance.

The adhesive performance of the sensor depends not only on substrate contact area but also on its intrinsic properties. Research has shown that, when calculating the horizontal shear force of a viscoelastic object, a critical shear force (F_C) exists, expressed as follows[57]:

$$F_C \sqrt{G_C}\sqrt{\frac{AE}{C}}$$

Where G_C represents the energy per unit area of contact between the sensor and substrate at the critical strain, depending on the geometry and material properties; A is the contact area between the sensor and substrate; E is the elastic modulus of the sensor; and C is the elastic potential energy storage capacity. Under identical substrate conditions, A, C, and G_C remain constant, so the critical shear force is primarily positively correlated with the sensor's elastic modulus E. To evaluate this relationship, a series of self-adhesive sensors were produced by electrospinning PDMA for varying durations on identical sensing and spacer layers, their E values were measured, and shear force tests were conducted on PTFE substrates. The results indicated that as the spinning time increased, the elastic modulus of the sensor significantly increased, and the shear force also correspondingly increased (Fig. S7). This finding further confirms the positive correlation between the sensor's adhesion performance and its elastic modulus.

The sensing layer, spacer layer, and adhesive layer of the self-adhesive sensor were all fabricated using electrospinning, forming a three-dimensional network structure, as shown in Fig. 2a–c. This architecture creates numerous interconnected channels within the sensor, ensuring adequate airflow and thereby imparting excellent breathability. To evaluate its air permeability, this study measured the air resistance (R_a) of TPU nonwoven elastomers, individual sensor layers, and the fully assembled sensor, and compared with with commercial fabrics. As illustrated in Fig. S8, R_a progressively increased with sensor fabrication, leading to decreased breathability. This phenomenon can be attributed to the partial blockage of channels by conductive materials in the sensing layer, as well as the reduced number of channels due to interlayer contact. Further analysis indicates that the sensor's breathability falls between that of purple elastic fabric and commercial single-layer knitted fabric, demonstrating superior air permeability sufficient for commercialization.

3.3. Sensing performance

Reliable mechanical performance is a crucial factor for the practical application of flexible sensors, as it directly affects their stability and operational lifespan [58–60]. Thermoplastic polyurethane (TPU), a block copolymer, comprises alternating hard and soft segments. The hard segments, typically consisting of isocyanates and chain extenders, impart rigidity and strength, while the soft segments, derived from polyester or polyether polyols, provide excellent elasticity and flexibility [61–63]. This unique molecular architecture enables TPU to dissipate stress effectively during tensile deformation, thereby exhibiting superior mechanical properties [64–66]. Accordingly, electrospun TPU nonwoven fabric was employed as the elastic substrate for the self-adhesive flexible sensor. As illustrated in Fig. 4a, the TPU nonwoven fabric exhibits a maximum tensile strain of approximately 382 %, a tensile strength of 1660.05 kPa, a toughness of 4524.09 kJ/m3, and a Young's modulus of 434.56 kPa. In comparison, the sensing layer demonstrates a similar maximum tensile strain of 385 %, yet with a higher tensile strength of 1937.16 kPa, a toughness of 5278.11 kJ/m3, and a Young's modulus of 503.15 kPa. Despite comparable strain limits, notable differences in other mechanical properties are observed. This discrepancy is primarily attributed to the conductive network formed by MWCNT/CB on the TPU fiber surface, which enhances the mechanical properties of the nonwoven fabric, whereas the intrinsic rigidity of MWCNT has a negligible effect on maximum tensile strain. Further electrospinning of spacer and adhesive layers onto the sensing layer results in a substantial improvement in mechanical performance. The fully assembled sensor exhibits a maximum tensile strain of approximately 547 %, a tensile strength of 2267.10 kPa, a toughness of 7017.85 kJ/m3, and a Young's modulus of 414.46 kPa. This enhancement is primarily due to extensive hydrogen bonding interactions within the PDMS-based adhesive layer, which strengthen intermolecular forces in TPU, thereby increasing tensile strength, toughness, and Young's modulus. Such a structural design not only optimizes the mechanical properties of the sensor but also ensures stable operation in complex environments. To ensure long-term operational stability the strain sensor must possess high toughness and resilience. As shown in Fig. 4b, cyclic tensile tests were conducted within a 0 to 100 % strain range for five cycles. The results indicate that even after five cycles at 100 % strain, the sensor exhibits minimal hysteresis and maintains stable

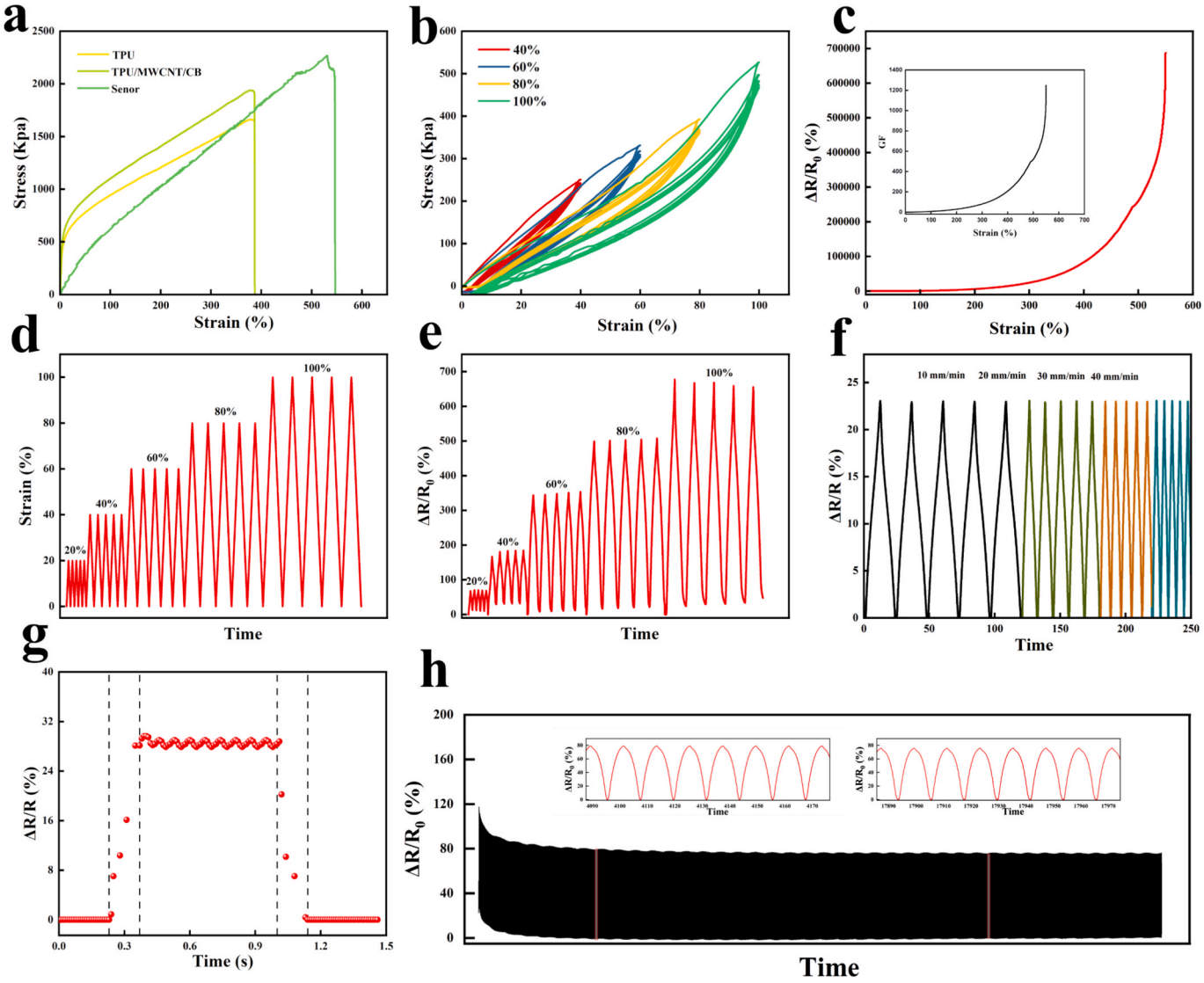

Fig. 4. a) Stress–strain curves of TPU elastomer, sensing layer, and self-adhesive sensor. b) Five-cycle stretching curve of the sensor within the 0 to 100 % strain range. c) Relationship between the sensor's $\Delta R/R_0$ and gauge factor (GF) with strain. d) Strain curve and e) Variation curve of $\Delta R/R_0$ with strain of the sensor in the 0 to 100 % strain range. f) $\Delta R/R_0$ variation curve of the sensor at different stretching rates within the 20 % strain range. g) Response and recovery time of the sensor. h) 2000-cycle stretching test of the sensor at 20 % strain.

performance. Given that human motion typically induces a maximum strain of approximately 55 % [22], the fabricated sensor fully meets the tensile performance requirements for human motion monitoring.

The sensing performance of the sensor relies on the conductive network formed by MWCNT/CB on TPU fibers. During tensile deformation, the relative resistance change ($\Delta R/R_0$, where ΔR is the resistance variation and R_0 is the initial resistanc) and sensitivity (gauge factor, GF) serve as key performance indicators. Based on preliminary studies, sensors with MWCNT concentrations ranging from 1 to 5 mg/mL were fabricated and subjected to resistance measurements, ultimately identifying 5 mg/mL as the optimal composition (Fig. S9a). However, due to the inherent rigidity of MWCNTs, their conductive network is prone to rupture under strain, leading to resistance values exceeding the measurable range (Fig. S9b). To enhance the stretchability of the conductive network, CB was introduced as interconnection points within the MWCNT framework. Sensors were fabricated by incorporating 1 to 5 mg/mL of CB into a 5 mg/mL MWCNT solution, followed by strain sensing tests in the 0 to100% strain range. The results indicate that when the CB content is 5 mg/mL, the sensor exhibits the highest sensitivity (Fig. S10a-e). Consequently, 5 mg/mL MWCNT/CB was selected as the conductive material for sensor fabrication.

A series of performance evaluations were conducted, including relative resistance variation, sensitivity, response time, and cyclic stability. As shown in Fig. 4c, the sensor exhibits a pronounced linear relationship between strain, relative resistance change, and sensitivity within the strain range of less than 100 % (Fig. S10f). This linearity arises from the fact that, within this range, deformation is primarily accommodated by the three-dimensional network of the TPU elastomer, with only minimal deformation occurring in the TPU fibers. In cyclic tensile tests conducted within the 0 to 100 % strain range, the peak resistance variation aligns synchronously with strain, demonstrating a stable and reliable response to complex stimuli (Fig. 4d and e). Additionally, under different stretching rates (10 to 40 mm/min), the sensor maintains stable peak resistance variations without noticeable electromechanical hysteresis (Fig. 4f). Benefiting from the fibrous structure and the excellent elasticity of TPU fibers, the response time of the sensor to strain variations is approximately 130 ms (Fig. 4g). Furthermore, after 2000 cycles at 20 % strain, no significant change in relative resistance variation was observed, indicating exceptional durability and repeatability. When the strain exceeds 100 %, the resistance and sensitivity of the sensor increase sharply (Fig. 4c). This phenomenon is attributed to TPU fibers bearing more strain, leading to rupture of the MWCNT/CB network and a decrease in conductive pathways, which causes a significant rise in resistance. In conclusion, the flexible strain sensor developed in this study demonstrates outstanding mechanical properties, sensing performance, and stability, making it fully suitable for human motion monitoring applications.

3.4. On-body experiment

During human signal acquisition, sensors were required to deliver high sensing performance while avoiding material migration or leakage in practical use. Furthermore, good biocompatibility was essential to prevent skin irritation. As shown in Fig. S11 and Video S1, the developed sensor exhibited no detectable leakage of functional materials under experimental conditions and did not induce skin irritation upon contact, confirming its reliable biosafety. To ensure accurate signal collection, the sensor must adhere stably to the skin surface. Conversely, due to the presence of fine wrinkles on the skin, shear forces along the horizontal direction are significantly greater than peel forces along the vertical direction. Consequently, the adhesive performance of the sensor on human skin is primarily reflected in its resistance to vertical peeling. Moreover, considering the wet environments encountered during human activities (such as perspiration or external moisture) the sensor's adhesion under wet conditions is also critical. The self-adhesive sensor developed in this study exhibits outstanding adhesion properties, effectively addressing these challenges. Fig. 5a–c and Video S2 illustrate the actual adhesion performance of the sensor on both dry and moist skin, clearly demonstrating its ability to effectively adhere to human skin. To further evaluate its adhesive properties, a flexible multimodal testing system was employed to measure and compare the vertical peeling force of medical tape and the sensor on the skin (Fig. S12). The results indicate that the peeling adhesion force of medical tape on dry skin is approximately 122N/m (Fig. S13a), while that of the sensor is around 118 N/m on dry skin and 48 N/m on wet skin (Fig. 5d). These findings demonstrate that the sensor exhibits comparable adhesion to medical tape, verifying its reliability for practical applications. Moreover, as discussed in Section 3.2, the sensor also possesses excellent breathability, further enhancing its potential for wearable applications.

In this study, copper foil electrodes were integrated at both ends of the sensor's sensing layer and connected to a Keithley digital source meter via conductive wiring for signal acquisition. By attaching the sensor to different parts of the human body, real-time monitoring and recognition of body movements can be achieved. The sensor's high Young's modulus enables effective detection of large-scale joint movements. For instance, when affixed to a volunteer's index finger joint for flexion monitoring (Fig. S12bI), the sensor's relative resistance change ($\Delta R/R_0$) exhibits a corresponding variation with different bending angles or fixed positions. As shown in Fig. 5e, when the index finger bends within the range of 0° to 90° (with a maximum bending angle of 90° for the volunteer tested, due to personal flexibility differences), the sensor's $\Delta R/R_0$ value varies from 0 % to 416 % accordingly. At specific bending angles of 10°, 20°, 40°, and 90°, $\Delta R/R_0$ stabilizes at 34 %, 71 %, 104 %, and 416 %, respectively. Furthermore, during rapid cyclic bending at fixed angles, the peak $\Delta R/R_0$ values remain consistent with those observed in static bending (Fig. 5f). Notably, due to the difficulty in precisely controlling finger bending angles and the presence of minor tremors, the sensor's signal curve exhibits slight jagged fluctuations, distinguishing it from the stable signals observed in mechanical tensile tests. Moreover, the sensor can be attached to joints such as the wrist, elbow, and knee to monitor joint movements(Fig. S13bII,III and IV). As shown, the sensor is capable of accurately distinguishing between various wrist joint bending angles (Fig. S13c) as well as detecting rapid cyclic bending at fixed elbow angles (Fig. 5g). In addition to measuring joint bending angles, the sensor is also capable of identifying movement frequency. Fig. 5h and 5i present the sensor response signals for rapid and slow bending of the wrist and knee, demonstrating that the $\Delta R/R_0$ peak values remain consistent at the same bending angle, with variations only in peak width. These results confirm the sensor's stable and repeatable response to joint motion, enabling effective detection of intense human activities. More importantly, the sensor can accurately determine the bending frequency of the wrist and knee by counting the number of response peaks over time and distinguish specific joints based on peak shape. These capabilities highlight the sensor's potential for applications in smart wearable devices for personal care and healthcare services, particularly for the elderly and individuals with disabilities.

To promote the widespread application of flexible sensors in human motion monitoring, this study proposes a machine learning algorithm based on a convolutional neural network (CNN), which was designed to process and recognize human motion signal data. The experimental process was as follows: initially, raw data corresponding to various joint movements and bending angles were acquired and preprocessed (Fig. 6a). The dataset was then partitioned into training (80 %) and testing (20 %) sets (Fig. 6b). Finally, a CNN classification algorithm was employed for model training and evaluation, with recognition accuracy assessed via a confusion matrix. In the first experiment motion data corresponding to nine distinct finger bending angles (10° ~ 90°) were collected, with 200 samples per angle. As shown in Fig. 6c, the CNN model achieves an accuracy of 98.8 % in recognizing the nine bending angles, primarily due to the distinct 10° intervals between them, which result in clearly distinguishable data features. To further validate the sensor's applicability, data from five representative motions (elbow

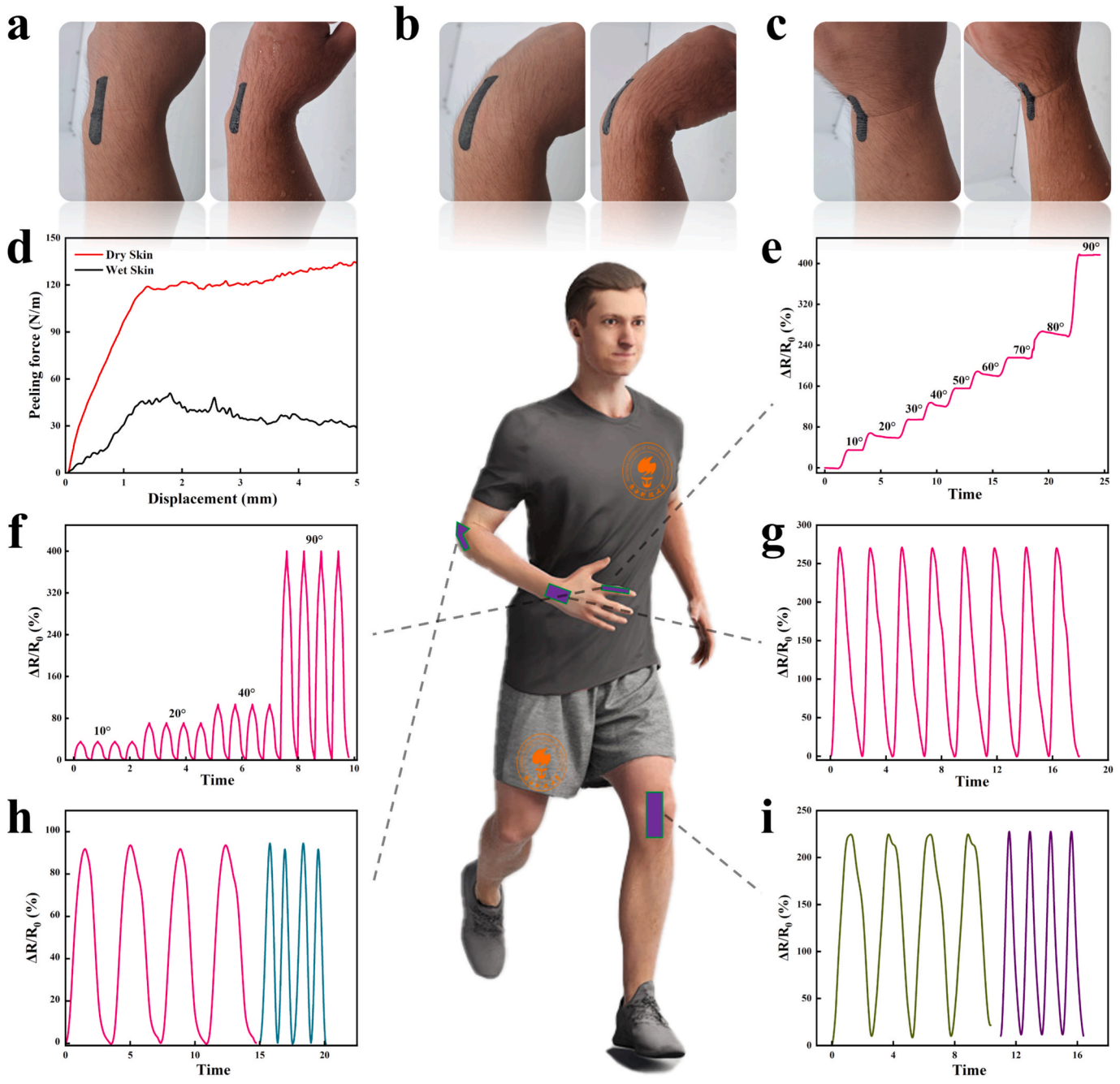

Fig. 5. a-c) The actual adhesion performance of the sensor on both dry (left) and wet (right) skin. d) Peel adhesion force tests of the sensor on dry and moist skin. Electrical response of the sensor to varying e) bending angles and f) rapid cyclic bending at fixed angles of the index finger. g) Electrical response of the sensor to rapid cyclic bending at a fixed angle of the elbow. Electrical response of the sensor to bending at different frequencies under a fixed angle of the h) wrist and i) knee.

bending, rapid/slow wrist bending, and rapid/slow knee bending) were collected (200 samples per motion) for training. As shown in Fig. 6d, the model achieves an overall recognition accuracy of 92.2 %. While the classification of different joint movements is highly accurate, there remains room for improvement in distinguishing between different movement frequencies. Increasing the training dataset is expected to further enhance the model's predictive performance. These findings underscore the significant potential of the proposed sensor for human motion monitoring applications.

With the evolving lifestyle of modern society, obesity has become an increasingly pressing issue, while traditional exercise routines often suffer from monotony, making long-term adherence challenging. To address this, thisstudy explores the potential application of the sensor in human–computer interaction systems. As illustrated in Fig. 6e, a motion-game interaction system was developed based on flexible sensors. The sensor is connected to a PCB with signal processing capabilities, which generates a 1 kHz, 5 V sinusoidal waveform applied to the sensor. When the sensor deforms, resistance changes modulate the output voltage, which is subsequently processed to control in-game actions (Fig. 6f). For instance, when attached to both index fingers (Fig. 6g), the sensor can be mapped to "jump" and "run" commands (Video S3); when affixed to the knee, it enables real-time synchronization between actual running motions and in-game character movements, significantly enhancing exercise engagement. In essence, the combination of human motion, flexible sensors, and PCB hardware functions analogously to a game controller (Fig. 6g). The present system still requires further optimization in terms

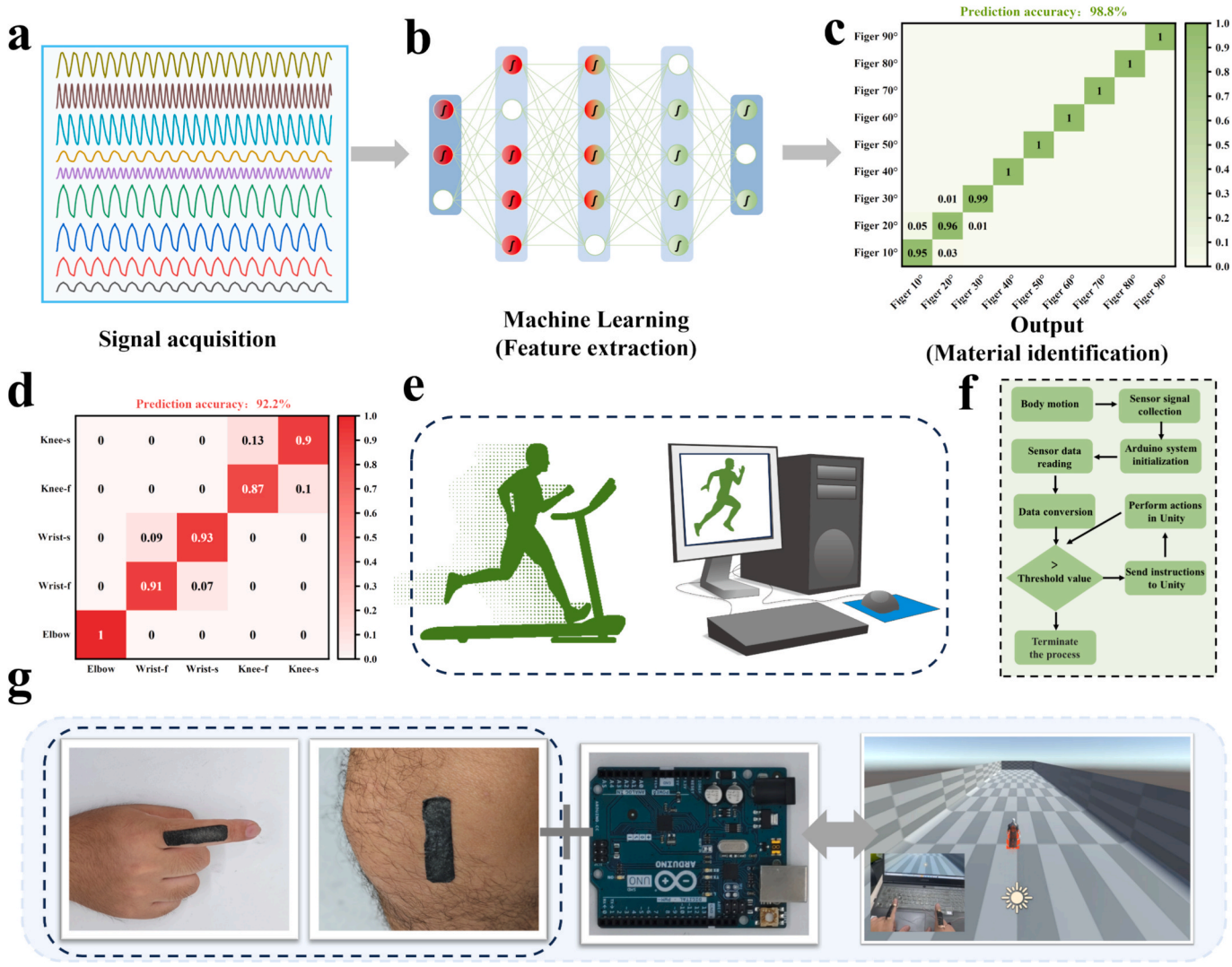

Fig. 6. a) Human motion data collected by the sensor. b) Flowchart of the machine learning algorithm based on convolutional neural networks (CNN) for recognizing human motion. Confusion matrix for validating c) finger bending angle and d) human joint recognition. e) Schematic diagram of human motion mapped to game character commands. f) Flowchart of the motion-to-game mapping process. g) Schematic diagram of the sensor with PCB integrated as an equivalent to a game controller.

of PCB durability and data transmission stability. Nevertheless, it has already demonstrated the great potential of flexible sensors for human–machine interaction. Compared with previously reported sensor systems, the proposed sensor exhibited greater comprehensiveness (Table S1). Therefore, with continued progress in system integration and algorithm optimization, more practical and intelligent motion-assist systems are expected to be developed in the future.

4. Conclusion

In summary, this study presents a self-adhesive flexible strain sensor fabricated via electrospinning, which simultaneously achieves strain sensing, self-adhesion on various substrates, breathability, and waterproof performance. The three-dimensional fibrous network generated by electrospinning imparts excellent breathability (0.06 kPa·S/m), comparable to commercial knitted fabrics. The PDMA adhesion layer ensures robust adhesion through strong intermolecular van der Waals forces, while the incorporation of poly (octadecyl acrylate) and poly (lauryl acrylate) enables tunable melting temperatures for controlled adhesion (strong adhesion at low temperatures and easy detachment at elevated temperatures). Additionally, these modifications impart hydrophobicity to the adhesive layer, ensuring stable adhesion even in humid environments (water contact angle: 107.2°). Comprehensive performance assessments indicate that the sensor's adhesion strength is positively correlated with the roughness and Young's modulus of the contact surface but negatively correlated with environmental humidity. Stability tests indicate that after 10 adhesion-detachment cycles and three days of adhesion on PTFE substrates, the adhesion strength fluctuations are less than 2.9 %, demonstrating exceptional durability. Human trials further confirm stable conformal contact, with peel adhesion forces of 118N/m and 48 N/m on dry and moist skin, respectively. Integrated with terminal devices and machine learning algorithms, the sensor enables accurate real-time motion recognition, achieving classification accuracies of 98.8 % in recognizing joint movements and 92.2 % accuracy in joint identification. Finally, a simplified motion-to-game interaction system was developed by integrating the sensor with a PCB, successfully mapping human motions to game control commands. These findings not only advance the development of high-precision wearable electronics but also pave the way for flexible sensors in applications such as digital healthcare and virtual reality.

CRediT authorship contribution statement

Xiaodong Wang: Writing – original draft, Formal analysis, Data

curation, Conceptualization. **Ziqian Bai:** Writing – review & editing, Supervision, Funding acquisition. **Kai Lin:** Data curation. **Hongci Hu:** Writing – review & editing, Formal analysis.

Declaration of competing interest

The authors declare that they have no known competing financial interests or personal relationships that could have appeared to influence the work reported in this paper.

Acknowledgments

The authors' work has been supported by the National Natural Science Foundation of China under Funding No. 52203312, Natural Science Foundation of Guangdong Province of China under Funding No. 2023A1515011282, and the Guangdong Science and Technology Program under Grant No. 2024B1212010002.

Appendix A. Supplementary data

Supplementary data to this article can be found online at https://doi.org/10.1016/j.matdes.2025.114694.

Data availability

Data will be made available on request.

References

[1] L.P. Liu, S.C. Niu, J.Q. Zhang, et al., Bioinspired, omnidirectional, and hypersensitive flexible strain sensors, Adv. Mater. 34 (17) (2022) 2200823.
[2] Q. Wang, Z.W. Yao, C.C. Zhang, et al., A selective-response hypersensitive bio-inspired strain sensor enabled by hysteresis effect and parallel through-slits structures, Nano-Micro Lett. 16 (1) (2024) 26.
[3] R.R. Zhao, J.X. Luo, J.C. Liu, et al., Ultra-flexible, anti-freezing, and adhesive collagen fiber-derived conductive organohydrogel e-skin for strain, humidity, temperature, and bioelectric sensing applications, Chem. Mater. 36 (17) (2024) 8141–8158.
[4] X.Y. Yue, C.Q. Fang, Q.Z. Yao, et al., Tunable porous fiber-shaped strain sensor with synergistic conductive network for human motion recognition and tactile sensing, Chem. Eng. J. 491 (2024) 151853.
[5] M.Z. Lin, Z.J. Zheng, L. Yang, et al., A high-performance, sensitive, wearable multifunctional sensor based on rubber/CNT for human motion and skin temperature detection, Adv. Mater. 34 (1) (2022) 2107309.
[6] Y. Yang, L. Wang, J.W. Zhang, et al., Multifunctional biomimetic e-skin constructed In situ on tanned sheep leather as a multimodal sensor for the monitoring of motion and health, Ind. Eng. Chem. Res. 63 (32) (2024) 14176–14189.
[7] T.X. Feng, D. Ling, C.Y. Li, et al., Stretchable on-skin touchless screen sensor enabled by ionic hydrogel, Nano Res. 17 (5) (2024) 4462–4470.
[8] W.Y. Wang, D.J. Yao, H. Wang, et al., A breathable, stretchable, and self-calibrated multimodal electronic skin based on hydrogel microstructures for wireless wearables, Adv. Funct. Mater. 34 (32) (2024) 2316339.
[9] B. Song, X.D. Dai, X. Fan, et al., Wearable multifunctional organohydrogel-based electronic skin for sign language recognition under complex environments, J. Mater. Sci. Technol. 181 (2024) 91–103.
[10] Z.Q. Shen, Z.L. Zhang, N.B. Zhang, et al., High-stretchability, ultralow-hysteresis conductingpolymer hydrogel strain sensors for soft machines, Adv. Mater. 34 (32) (2022) 2203650.
[11] Y. Liu, G.X. Tian, Y.J. Du, et al., Highly stretchable, low-hysteresis, and adhesive TA@MXene-composited organohydrogels for durable wearable sensors, Adv. Funct. Mater. 34 (30) (2024) 2315813.
[12] X. Shi, J.L. Shen, J.W. Zhang, et al., Transparent materials top-down constructed by using animal skins for light management application, Ind. Eng. Chem. Res. 63 (50) (2024) 21942–21959.
[13] S. Wang, Y.L. Fang, H. He, et al., Wearable stretchable dry and self-adhesive strain sensors with conformal contact to skin for high-quality motion monitoring, Adv. Funct. Mater. 31 (5) (2021) 2007495.
[14] C.J. Zhu, G.Q. Chen, S.N. Li, et al., Breathable ultrathin film sensors based on nanomesh reinforced anti-dehydrating organohydrogels for motion monitoring, Adv. Funct. Mater. 34 (52) (2024) 2411725.
[15] H. Liu, S.Y. Yan, W. Wang, et al., Ultra-tough multifunctional teather-based e-skin as sensitive multimodal sensors for strain, temperature, humidity, and bioelectrical signals, Ind. Eng. Chem. Res. 64 (17) (2025) 8787–8804.
[16] Z.K. Liu, T.X. Zhu, J.R. Wang, et al., Functionalized fiber-based strain sensors: pathway to next-generation wearable electronics, Nano-Micro Lett. 14 (1) (2022) 61.
[17] Q.Y. Song, K. Wang, G. Zhao, Self-adhesive, conductive, and antibacterial hydrogel nanofiber composite as a flexible strain sensor, ACS Appl. Electron. Mater. 5 (12) (2023) 6947–6954.
[18] X. Shi, M.H. Lan, J.C. Liu, et al., Highly robust, self-adhesive, self-healing, pH-responsive, cytocompatible and degradable collagen/PVA/tannin-based conductive hydrogel sensor for motion-monitoring, Polymer 308 (2024) 127365.
[19] Y. Qiu, Y. Tian, S.S. Sun, et al., Bioinspired, multifunctional dual -mode pressure sensors as electronic skin for decoding complex loading processes and human motions, Nano Energy 78 (2020) 105337.
[20] S. Sakaguchi, K. Saito, N. Arakawa, et al., The dynamic behavior of skin in response to vibrating touch stimuli affects tactile perception, Skin Res. Technol. 29 (3) (2023) e13295.
[21] J.L. Shen, Y. Yang, J.W. Zhang, et al., Carbon quantum dot-functionalized dermis-derived transparent electronic skin for multimodal human motion signal monitoring and construction of self-powered triboelectric nanogenerator, ACS Appl. Mater. Interfaces 16 (35) (2024) 46771–46788.
[22] J.H. Kim, K.G. Cho, D.H. Cho, et al., Ultra-sensitive and stretchable ionic skins for high-precision motion monitoring, Adv. Funct. Mater. 31 (16) (2021) 2010199.
[23] Y.D. Chen, C.H. Lv, X.L. Ye, et al., Hydrogel-based pressure sensors for electronic skin systems, Matter 8 (3) (2025) 101992.
[24] Q.T. Lai, X.H. Zhao, Q.J. Sun, et al., Emerging MXene-based flexible tactile sensors for health monitoring and haptic perception, Small 19 (27) (2023) 2300283.
[25] S.Y. Liu, Y.F. Rao, H. Jang, et al., Strategies for body-conformable electronics, Matter 5 (4) (2022) 1104–1136.
[26] G.F. Sun, P. Wang, Y.X. Jiang, et al., Bioinspired flexible, breathable, waterproof and self-cleaning iontronic tactile sensors for special underwater sensing applications, Nano Energy 110 (2023) 108367.
[27] Z. Yuan, H. Li, Z.H. Duan, et al., High sensitivity, wide range and waterproof strain sensor with inner surface sensing layer for motion detection and gesture reconstruction, Sens. Actuat. A-Phys. 369 (2024) 115202.
[28] G. Li, C.L. Li, G.D. Li, et al., Development of conductive hydrogels for fabricating flexible strain sensors, Small 18 (5) (2022) 2101518.
[29] X.W. Xu, Y.C. Chen, P. He, et al., Wearable CNT/Ti3C2Tx MXene/PDMS composite strain sensor with enhanced stability for real-time human healthcare monitoring, Nano Res. 14 (8) (2021) 2875–2883.
[30] G. Li, Y.S. Xue, H. Peng, et al., Wide strain range and high sensitivity sandwich structure CNTs/AgNWs/ CNTs/TPU strain sensors for human motion detection, Sens. Actuat. A-Phys. 366 (2024) 114998.
[31] R.G. Ferreira, A.P. Silva, J. Nunes-Pereira, Current on-skin flexible sensors, materials, manufacturing approaches, and study trends for health monitoring: a review, Acs Sens. 9 (3) (2024) 1104–1133.
[32] L. Han, X. Lu, K.Z. Liu, et al., Mussel-inspired adhesive and tough hydrogel based on nanoclay confined dopamine polymerization, ACS Nano 11 (3) (2017) 2561–2574.
[33] X.Y. Zhang, F. Li, S.Y. Liang, et al., Sweat-enhanced adhesive hydrogel enables interfacial exchange coupling for wearable strain sensor, Chem. Eng. J. 495 (2024) 153385.
[34] E. Filippidi, T.R. Cristiani, C.D. Eisenbach, et al., Toughening elastomers using mussel-inspired iron-catechol complexes, Science 358 (6362) (2017) 502–505.
[35] W.C. Zhao, H.F. Zhou, W.K. Li, et al., An environment-tolerant ion-conducting double-network composite hydrogel for high-performance flexible electronic devices, Nano-Micro Lett. 16 (1) (2024) 99.
[36] Z. He, J.L. Shen, M.H. Lan, et al., Collagen fiber-reinforced, tough and adaptive conductive organohydrogel e-skin for multimodal sensing applications, J. Mater. Chem. B 12 (28) (2024) 6940–6958.
[37] J.C. Liu, X. Fan, D. Astruc, et al., Robust conductive skin hydrogel e-skin constructed by top-down strategy for motion-monitoring, Collagen Leather 5 (1) (2023) 17.
[38] X. Yao, S.F. Zhang, L.W. Qian, et al., Super stretchable, self-healing, adhesive ionic conductive hydrogels based on tailor-made ionic liquid for high-performance strain sensors, Adv. Funct. Mater. 32 (33) (2022) 2204565.
[39] D. Tan, F.D. Meng, Y.X. Ni, et al., Robust and smart underwater adhesion of hydrophobic hydrogel by phase change, Chem. Eng. J. 471 (2023) 144625.
[40] B. Song, J.L. Shen, X. Shi, et al., Antibacterial, antifreezing, and tough electronic skin based on a tanned collagen fiber network for underwater grabber application, ACS Appl. Mater. Interfaces 17 (27) (2025) 39561–39575.
[41] A. Huang, Y. Guo, Y.W. Zhu, et al., Durable washable wearable antibacterial thermoplastic polyurethane/carbon nanotube@silver nanoparticles electrospun membrane strain sensors by multi-conductive network, Adv. Compos. Hybrid Mater. 6 (3) (2023) 101.
[42] J. Lin, J.W. Li, W. Li, et al., Multifunctional polyimide nanofibrous aerogel sensor for motion monitoring and airflow perception, Compos. Pt. A-Appl. Sci. Manuf. 178 (2024) 108003.
[43] G.X. Luo, J.Q. Xie, J.L. Liu, et al., Highly conductive, stretchable, durable, breathable electrodes based on electrospun polyurethane mats superficially decorated with carbon nanotubes for multifunctional wearable electronics, Chem. Eng. J. 451 (2023) 138549.
[44] Y. Tian, M.J. Huang, Y.L. Wang, et al., Ultra-stretchable, sensitive and breathable electronic skin based on TPU electrospinning fibrous membrane with microcrack structure for human motion monitoring and self-powered application, Chem. Eng. J. 480 (2024) 147899.
[45] X.F. Pan, Q.H. Wang, P. He, et al., A bionic tactile plastic hydrogel-based electronic skin constructed by a nerve-like nanonetwork combining stretchable, compliant, and self-healing properties, Chem. Eng. J. 379 (2020) 122271.

[46] K. Chen, K.W. Liang, H. Liu, et al., Skin-inspired ultra-tough supramolecular multifunctional hydrogel electronic skin for human-machine interaction, Nano-Micro Lett. 15 (1) (2023) 102.
[47] K. Kang, S. Ye, C. Jeong, et al., Bionic artificial skin with a fully implantable wireless tactile sensory system for wound healing and restoring skin tactile function, Nat. Commun. 15 (1) (2024) 10.
[48] H. Zhang, J.H. Guo, Y. Wang, et al., Stretchable and conductive composite structural color hydrogel films as bionic electronic skins, Adv. Sci. 8 (20) (2021) 2102156.
[49] M. Lei, K. Feng, S. Ding, et al., Breathable and waterproof electronic skin with three-dimensional architecture for pressure and strain sensing in nonoverlapping mode, ACS Nano 16 (8) (2022) 12620–12634.
[50] M.C. Qu, L.Z. Hu, S.Y. Wang, et al., Multifunctional hierarchical electronic skins: unveiling self-repairing mechanisms and advancements in sensing and shielding performance, Compos. Sci. Technol. 256 (2024) 110769.
[51] C.D. Zhang, X. Yang, L.D. Yu, et al., Electrospun polyasparthydrazide nanofibrous hydrogel loading with in-situ synthesized silver nanoparticles for full-thickness skin wound healing application, Mater. Des. 239 (2024) 112818.
[52] W.W. Li, J. Liu, J.N. Wei, et al., Recent progress of conductive hydrogel fibers for flexible electronics: fabrications, applications, and perspectives, Adv. Funct. Mater. 33 (17) (2023) 2213485.
[53] S. Jin, H. Jung, J. Song, et al., Adhesive and Conductive fibrous hydrogel bandages for effective peripheral nerve regeneration, Adv. Healthc. Mater. (2025) 2403722.
[54] X. He, Z.K. Li, J. Li, et al., Ultrastretchable, adhesive, and antibacterial hydrogel with robust spinnability for manufacturing strong hydrogel micro/nanofibers, Small 17 (49) (2021) 2103521.
[55] Y.N. Hao, Q.Y. Yan, H.J. Liu, et al., A stretchable, breathable, and self-adhesive electronic skin with multimodal sensing capabilities for human-centered healthcare, Adv. Funct. Mater. 33 (44) (2023) 2303881.
[56] D. Tan, X.Y. Guan, K.Y. Chung, et al., Smart-adhesive, breathable and waterproof fibrous electronic skins, Adv. Sci. 11 (36) (2024) 2405828.
[57] M.D. Bartlett, A.B. Croll, D.R. King, et al., Looking beyond fibrillar features to scale gecko-like adhesion, Adv. Mater. 24 (8) (2012) 1078–1083.
[58] J.C. Dong, D. Wang, Y.D. Peng, et al., Ultra-stretchable and superhydrophobic textile-based bioelectrodes for robust self-cleaning and personal health monitoring, Nano Energy 97 (2022) 107160.
[59] Z.Y. Gao, X. Xiao, A.D. Carlo, et al., Advances in wearable strain sensors based on electrospun fibers, Adv. Funct. Mater. 33 (18) (2023) 2214265.
[60] M.A.U. Khalid, S.H. Chang, Flexible strain sensors for wearable applications fabricated using novel functional nanocomposites: a review, Compos. Struct. 284 (2022) 115214.
[61] S.M. Desai, R.Y. Sonawane, A.P. More, Thermoplastic polyurethane for three-dimensional printing applications: a review, Polym. Adv. Technol. 34 (7) (2023) 2061–2082.
[62] T.J. Chen, Y.T. Xie, Z.Y. Wang, et al., Recent advances of flexible strain sensors based on conductive fillers and thermoplastic polyurethane matrixes, ACS Appl. Polym. Mater. 3 (11) (2021) 5317–5338.
[63] T.K. Kim, B.K. Kim, S.Y. Lee, et al., Thermoplastic polyurethane elastomer/thermoplastic polyolefin elastomer blends compatibilized with a polyolefinic segment in TPU, Macromol. Res. 18 (2) (2010) 177–184.
[64] M. Kannan, S.S. Bhagawan, K. Joseph, et al., Mechanical properties and morphology of nanoclay filled different TPU/PP blend nanocomposites: structure - property relations, J. Compos. Mater. 43 (18) (2009) 1915–1925.
[65] F. Lu, Y. Liu, S.X. Gao, et al., SEBS-b-TPU and nanoclay: effective compatibilizers for promotion of the interfacial adhesion and properties of immiscible SEBS/TPU blends, Polym. Bull. 78 (6) (2021) 3293–3310.
[66] C. Zhang, M.N. Shi, Y.C. Zhang, et al., EG/TPU composites with enhanced flame retardancy and mechanical properties prepared by microlayer coextrusion technology, RSC Adv. 9 (41) (2019) 23944–23956.